Communication



# Nonlinear Thermal Drift Characteristics in Temperature-Insensitive Silicon Nitride Microring Resonators

Tiangang Zheng , Rui Yin , Jian Xin , Shuai Li , Ming Li , Xin Wang *

Posted Date: 5 March 2026

doi: 10.20944/preprints202603.0422.v1

Keywords: athermal; microring resonators; photoelastic effect; silicon nitride; polymethyl methacrylate

 doi:10.20944/preprints202603.0422.v1



*Communication*

# Nonlinear Thermal Drift Characteristics in Temperature-Insensitive Silicon Nitride Microring Resonators

**Tiangang Zheng [1,2,3], Rui Yin [1,2,3], Jian Xin [4], Shuai Li [4], Ming Li [1,2,3] and Xin Wang [1,2,3,*]**

[1] State Key Laboratory of Optoelectronic Materials and Devices, Institute of Semiconductors, Chinese Academy of Sciences, Beijing 100083, China

[2] School of Electronic, Electrical and Communication Engineering, University of Chinese Academy of Sciences, Beijing 100049, China

[3] College of Materials Science and Opto-Electronic Technology, University of Chinese Academy of Sciences, Beijing 100049, China

[4] Yongjiang Laboratory

* Correspondence: wxin@semi.ac.cn

**Abstract**

The thermal drift of microring resonators is one of the key obstacles hindering their practical applications. Employing polymers with negative thermo-optic coefficients to compensate for temperature-induced wavelength shifts represents a common solution. This study utilizes polymethyl methacrylate (PMMA) to compensate silicon nitride microring resonators, achieving thermal drift magnitudes below 2.0 pm/K within the temperature range of 15℃ to 70℃. Furthermore, nonlinear thermal drift characteristics were experimentally observed, and simulations revealed that these nonlinearities primarily originate from the temperature-dependent Young's modulus and Poisson's ratio of PMMA. This research provides design references for waveguide compensation using negative thermo-optic coefficient materials and proposes a conceptual framework for dual-function devices capable of both athermal operation and thermal tuning.

**Keywords:** athermal; microring resonators; photoelastic effect; silicon nitride; polymethyl methacrylate

## 1. Introduction

The microring structures exhibit broad applications in fields such as communication, sensing, and optical computing. However, constrained by current fabrication processes and their inherent temperature-sensitive characteristics, microring structures still face critical challenges in the commercialization process. Even with temperature control mechanisms implemented, significant time delays hinder timely correction of thermal drift [1]. Therefore, achieving passive low thermal drift has become a crucial technical challenge for promoting large-scale commercialization of microring devices.

The temperature sensitivity of microring structures primarily originates from the thermo-optic effect of dielectric materials, typically characterized by a positive thermo-optic coefficient where the refractive index increases with rising temperature, consequently causing redshift in the resonance wavelength. To suppress this thermal drift, current mainstream research approaches focus on introducing compensating materials with negative thermo-optic coefficients to enhance temperature stability through mutual compensation of their thermo-optic effects. Among materials exhibiting negative thermo-optic coefficients, titanium dioxide ($TiO_2$) has attracted significant attention due to its high mechanical strength, stable performance, and compatibility with CMOS processes. By employing magnetron sputtering technology, uniform $TiO_2$ thin films can be fabricated on silicon

 doi:10.20944/preprints202603.0422.v1



surfaces, and appropriate design of waveguide dimensions enables achievement of near-zero thermal drift in silicon microrings [2–4]. Chalcogenide compounds possess low optical loss; studies have demonstrated that optimizing cladding layer thickness can achieve resonance wavelength thermal drift as low as ~5.25 pm/K in silicon microrings [5]. Additionally, research utilizing plasma-enhanced chemical vapor deposition (PECVD) to deposit silicon dioxide under varying temperature conditions has modified the effective refractive index of waveguides, successfully controlling the resonance wavelength thermal drift of microring structures within the range of +29.5 pm/K to -118 pm/K [6]. Polymers represent another class of commonly used thermo-optic effect compensation materials, characterized by simple fabrication processes and ease of integration [7–17]. Various polymeric materials including polymethyl methacrylate (PMMA) [7–11], ethylene oxide [13], polyurethane acrylate (PUA) [14,17], polycarbonate [15] and silicone resin [11] have been widely adopted in microrings, successfully achieving microring structures with low thermal drift characteristics.

A scheme employing PMMA to compensate for the thermo-optic effect in silicon nitride ($Si_3N_4$), thereby achieving low thermal drift in silicon nitride microring resonators, has been previously proposed [7]. This study fabricated the microring resonators with PMMA-cladding silicon nitride waveguide. For these microring resonators, low wavelength thermal drift was validated within the 15°C to 70°C range. While the absolute value of wavelength thermal drift remained below 2.0 pm/K across this temperature interval, a distinct nonlinear thermal drift characteristic was identified: the thermal drift magnitude first increased and subsequently decreased with rising temperature. To elucidate the underlying mechanism of this phenomenon, finite element method (FEM) simulations were conducted. The study provides design guidelines for such compensation strategies and proposes potential applications based on this observed behavior.

## 2. Materials and Methods

When electromagnetic field propagates within an optical waveguide, a portion of waveguide mode penetrates into the cladding and substrate. The electromagnetic fields distributed across the cladding, substrate, and core regions collectively influence the effective refractive index of the waveguide. Consequently, the temperature-dependent refractive index variations in these regions jointly affect the thermal response of the waveguide's effective refractive index, which can be mathematically described by Equation (1) [10].

$$\frac{\partial n_{eff}}{\partial T} = \Gamma_{core}\frac{\partial n_{core}}{\partial T} + \Gamma_{clad}\frac{\partial n_{clad}}{\partial T} + \Gamma_{sub}\frac{\partial n_{sub}}{\partial T} \quad (1)$$

Here, $n_{eff}$ represents the effective refractive index of the waveguide. For the waveguide, $n_{core}$, $n_{clad}$ and $n_{sub}$ denote the refractive index of the core, cladding and the substrate respectively, T denotes the temperature, and $\Gamma_{core}$, $\Gamma_{clad}$ and $\Gamma_{sub}$ signifies the mode confinement factor of the core, cladding and the substrate respectively. The relationship between material refractive index variation and temperature is determined by material properties, while the mode confinement factor depends on optical wavelength, refractive index contrast, and waveguide structure. For the waveguide design in this study, the FEM was employed. First, by specifying the optical frequency and material properties, the eigen-propagation constants of the waveguide under different temperatures were calculated, thereby establishing the temperature-dependent effective refractive index relationship. Through parametric sweeping of waveguide parameters, the structural parameters corresponding to specified effective refractive index thermal drift could be obtained. After determining the waveguide structural parameters such as width and thickness, radius of the microring can be determined. based on the required resonant wavelength value, Free Spectral Range (FSR), and the obtained temperature-dependent effective refractive indices at different wavelengths. Subsequently, the directional coupler structure of the microring was modeled and simulated using the FEM to determine its coupling efficiency. The gap between the microring and input/output waveguides was then established according to waveguide loss characteristics and critical coupling conditions.

 doi:10.20944/preprints202603.0422.v1



This study designed two types of silicon nitride waveguide microring resonators, with the chip photograph shown in Figure 1(c). One type is a conventional silicon nitride microring resonator with a silica cladding layer, whose waveguide cross-sectional schematic is illustrated in Figure 1(a). The other type is a negative thermo-optic effect material-compensated microring resonator with a PMMA cladding layer, whose waveguide cross-sectional schematic is presented in Figure 1(b).

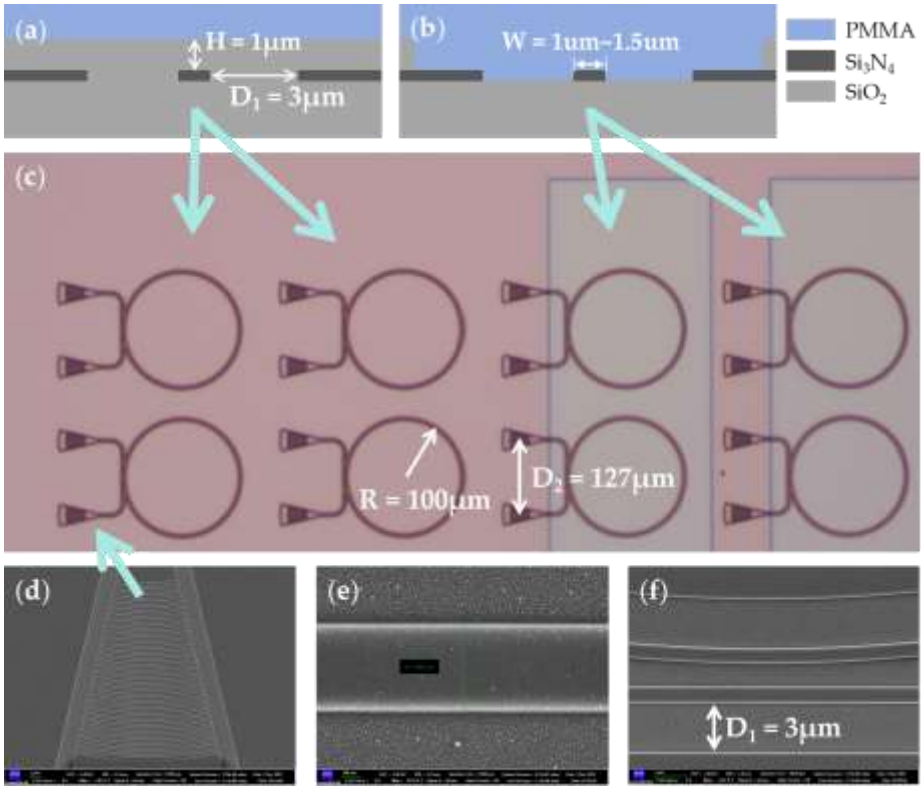


**Figure 1.** The designed microring resonators: (**a**) Schematic cross-sectional view of a conventional silicon nitride waveguide; (**b**) Schematic cross-sectional view of a negative thermo-optic effect material-compensated waveguide with PMMA cladding; (**c**) Photographs of the two types of microring resonators on the chip; (**d**) Grating coupler structure used for optical input/output of the microring; (**e**) Photograph of a 1μm-wide silicon nitride waveguide; (**f**) Photograph of the microring coupling structure.

The waveguides of the microrings have multiple widths including 1 μm, 1.2 μm and 1.5 μm, while maintaining a uniform radius R = 100 μm for all microrings. Both input and output coupling were implemented using grating couplers with a center wavelength of 1550 nm, as depicted in Figure 1(d), where the grating coupler spacing $D_2$ is 127 μm to facilitate fiber array coupling. All silicon nitride structures were fabricated through a process involving electron-beam lithography (EBL) followed by inductively coupled plasma (ICP) etching of a 300nm-thick silicon nitride layer. To reduce cost and fabrication time associated with positive resist patterning, exposure and etching were confined to a $D_1$ of 3 μm region on both sides of the waveguide, as shown in Figure 1(f). After etching of silicon nitride, a 1 μm-thick silica layer was deposited via PECVD, followed by partial removal of the silica layer above certain microring areas through ultraviolet photolithography and ICP etching. Finally, thickness of 2 μm PMMA-based EBL resist was spin-coated onto the chip surface and subsequently cured.

## 3. Results

During the preliminary simulation process, the temperature characteristics of the effective refractive indices for four types of waveguides were obtained. These waveguides include a conventional silicon nitride waveguide and PMMA-cladding waveguides with widths of 1 μm, 1.2 μm, and 1.5 μm, respectively. Based on the temperature dependence of the effective refractive indices,

 doi:10.20944/preprints202603.0422.v1



the thermal behavior of the microring resonant wavelength can be derived, which is presented in Figure 2.

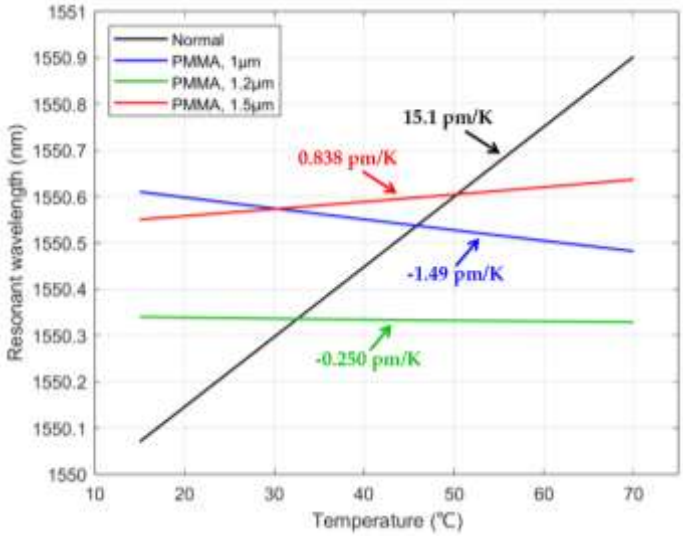


**Figure 2.** For 4 types of waveguide structures, the thermal drift characteristics of the corresponding microring resonators.

The simulation results demonstrate that microring resonators composed of PMMA-cladding waveguides exhibit significantly lower absolute values of temperature drift, with a temperature drift as low as -0.250 pm/K when the silicon nitride waveguide width is 1.2 μm, thereby proving the feasibility of this approach for realizing microring resonators with low thermal drift.

Subsequently, the fabricated microring resonators were tested. Experiment employed a wavelength swept laser and photodetector to obtain the frequency response curves of microring resonators. The laser model used was Santec TSL-570, with polarization control achieved using a Santec PCU-100 controller and optical power measurements performed by a Santec MPM-210H power meter. The wavelength measurement range was set from 1548 nm to 1552 nm with a resolution of 0.2 pm, while the laser output power was fixed at 10 dBm. The experimental temperature range extended from 15°C to 70°C, maintained by a thermoelectric cooler (TEC)-based temperature control platform where the chip was mounted, as illustrated in Figure 3(a). The input and output coupling of the chip were implemented through a 2-channel fiber array.

The measured wavelength responses of the three types of microring resonators are shown in Figure 3(b). It can be observed that for identical silicon nitride waveguides on the same chip, the performance of microring resonators with PMMA cladding does not exhibit significant degradation compared to those with silicon dioxide cladding. The thermal drift characteristics of conventional silicon nitride microring resonators and negative thermo-optic effect PMMA material-compensated silicon nitride microring resonators with waveguide widths of 1 μm, 1.2 μm, and 1.5 μm are presented in Figure 3(c). The conventional silicon nitride microring resonator shows a thermal drift of 14.9 pm/K, with its resonant wavelength variation demonstrating good linearity against temperature changes. In contrast, the resonance wavelength variations of the negative thermo-optic effect PMMA material-compensated silicon nitride microring resonators exhibit pronounced nonlinearity. Specifically, their thermal drift initially increases with rising temperature, but after exceeding a critical temperature between 40°C to 50°C, the thermal drift begins to decrease as temperature increases continuously. Within the temperature range of 15°C to 70°C: For the 1 μm waveguide width case, the thermal drift first increases to a maximum value of -0.6 pm/K and subsequently decreases to a minimum of -11.4 pm/K. For the case of 1.2 μm waveguide width, two athermal points exist, with the thermal drift increasing from a minimum of -2.8 pm/K to a maximum of 0.5 pm/K before continuously decreasing. For the case of 1.5 μm waveguide width , one athermal

 doi:10.20944/preprints202603.0422.v1



point exists, where the thermal drift increases from a minimum of -1.2 pm/K to a maximum of 2.0 pm/K before progressively decreasing.

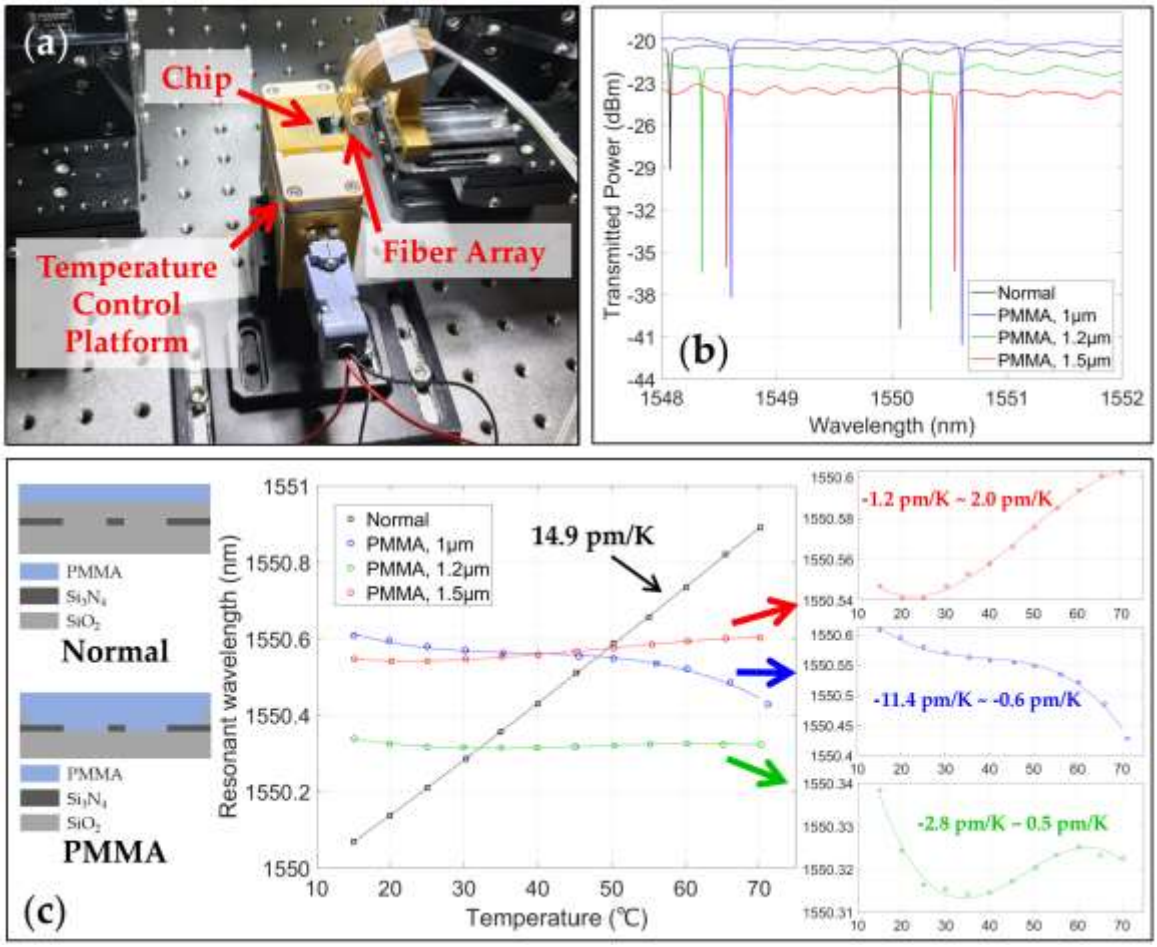


**Figure 3.** Experimental results: (**a**) Photo of the experiment site; (**b**) Measured frequency response curves of 4 types of microring resonators; (**c**) Measured thermal drift characteristics of 4 types of microring resonators, with the magnified views of PMMA-cladding microring resonators' thermal drift characteristics.

## 4. Discussion

For general free-standing bulk materials, their thermo-optic effect is primarily caused by the combined influence of temperature-dependent polarizability and thermal expansion effects, which can be described by Equation (2).

$$\frac{\partial n}{\partial T} = \left(\frac{\partial n}{\partial T}\right)_{\text{Polarizability}} + \left(\frac{\partial n}{\partial T}\right)_{\text{Thermal Expansion}} \quad (2)$$

Typically, as temperature increases, the material's polarizability rises, contributing positively to the refractive index, while the material's volume expansion reduces its density, resulting in a negative contribution to the refractive index. For PMMA, which possesses a large coefficient of thermal expansion (CTE) of approximately 75 ppm/K, the thermal expansion dominates the temperature-induced refractive index drift, leading to a negative thermo-optic coefficient. These two effects remain nearly constant within the room temperature range. As for PMMA, its coefficient of thermal expansion gradually increases with rising temperature. Therefore, under this condition, the resonant wavelength of the PMMA-compensated microring resonator exhibits a nearly linear response to temperature variations, while the thermal drift decreases slowly with increasing temperature. This behavior contradicts the experimentally observed phenomenon where the thermal drift initially increases and subsequently decreases with temperature elevation.

 doi:10.20944/preprints202603.0422.v1



When a material is constrained in its surrounding environment, its thermal expansion behavior will be affected, thereby generating thermal stress. First, consider a simplified model where five faces of a cube are constrained while the sixth face remains free. According to the generalized Hooke's law, these parameters can be formulated into the mathematical expression presented in Equation (3).

$$\begin{cases} \varepsilon_{sx} = \frac{1}{Y}[\sigma_x - \upsilon(\sigma_y + \sigma_z)] + \alpha_{CTE}\Delta T \\ \varepsilon_{sy} = \frac{1}{Y}[\sigma_y - \upsilon(\sigma_x + \sigma_z)] + \alpha_{CTE}\Delta T \\ \varepsilon_{sz} = \frac{1}{Y}[\sigma_z - \upsilon(\sigma_y + \sigma_x)] + \alpha_{CTE}\Delta T \end{cases} \tag{3}$$

where $\alpha_{CTE}$ denotes the coefficient of thermal expansion (CTE), Y represents Young's modulus, $\upsilon$ symbolizes Poisson's ratio, $\varepsilon_s$ indicates strain, and $\sigma$ signifies stress. Let the x-axis align with the normal direction of the free surface, resulting in stress-free conditions along the x-direction and strain-free conditions along both the y and z directions. Substituting these boundary conditions into Equation (3) yields the thermal stresses along the y and z directions given by Equation (4).

$$\sigma_y = \sigma_z = -\frac{Y\alpha_{CTE}\Delta T}{\upsilon - 1} \tag{4}$$

Simultaneously, the thermal strain along the x-direction can be obtained as shown in Equation (5).

$$\varepsilon_{sx} = \frac{1+\upsilon}{1-\upsilon}\alpha_{CTE}\Delta T \tag{5}$$

The relationship between refractive index and strain can be described by the photoelastic effect. For isotropic materials, the photoelastic effect can be expressed by Equation (6).

$$\begin{cases} n_x - n_0 \approx -\frac{n_0^3}{2}[p_{11}\varepsilon_{sx} + p_{12}(\varepsilon_{sy} + \varepsilon_{sz})] \\ n_y - n_0 \approx -\frac{n_0^3}{2}[p_{11}\varepsilon_{sy} + p_{12}(\varepsilon_{sx} + \varepsilon_{sz})] \\ n_z - n_0 \approx -\frac{n_0^3}{2}[p_{11}\varepsilon_{sz} + p_{12}(\varepsilon_{sy} + \varepsilon_{sx})] \end{cases} \tag{6}$$

The strain-optic coefficients at a certain point are denoted as $p_{11}$ and $p_{12}$.

Some studies have indicated that both Young's modulus and Poisson's ratio of PMMA material exhibit significant variations with increasing temperature [18,19]. Below the glass transition temperature, Young's modulus decreases as temperature rises, while Poisson's ratio demonstrates nonlinear increases with temperature elevation. Within the temperature range of 15℃ to 70℃, the rate of increase for Poisson's ratio accelerates with rising temperature [18]. Figure 4(d) presents the fitted temperature-dependent Poisson's ratio curve based on experimental data from other study [18]. Consequently, according to Equations (5) and (6), the refractive index will vary nonlinearly with temperature, which leads to nonlinear thermal drift in microring resonators. In practical scenarios, the stress and strain distributions are substantially more complex than those predicted by the aforementioned simplified model. Therefore, it is necessary to employ FEM to conduct coupled mechanical and electromagnetic field simulations for comprehensive investigation of the nonlinear temperature-dependent behavior of microring resonators' thermal drift under these considered factors.

For FEM simulations, the stress and strain distributions within the waveguide structure were first calculated. Once the strain distribution was obtained, it was used to compute the refractive index distribution. Subsequently, modal analysis was performed to extract the effective refractive index, which was then employed to determine the resonant wavelength values. Based on the temperature characteristics of the simulated effective refractive index combined with experimental measurements, unknown parameters were optimized to ultimately produce the simulation results shown in Figure 4.

 doi:10.20944/preprints202603.0422.v1



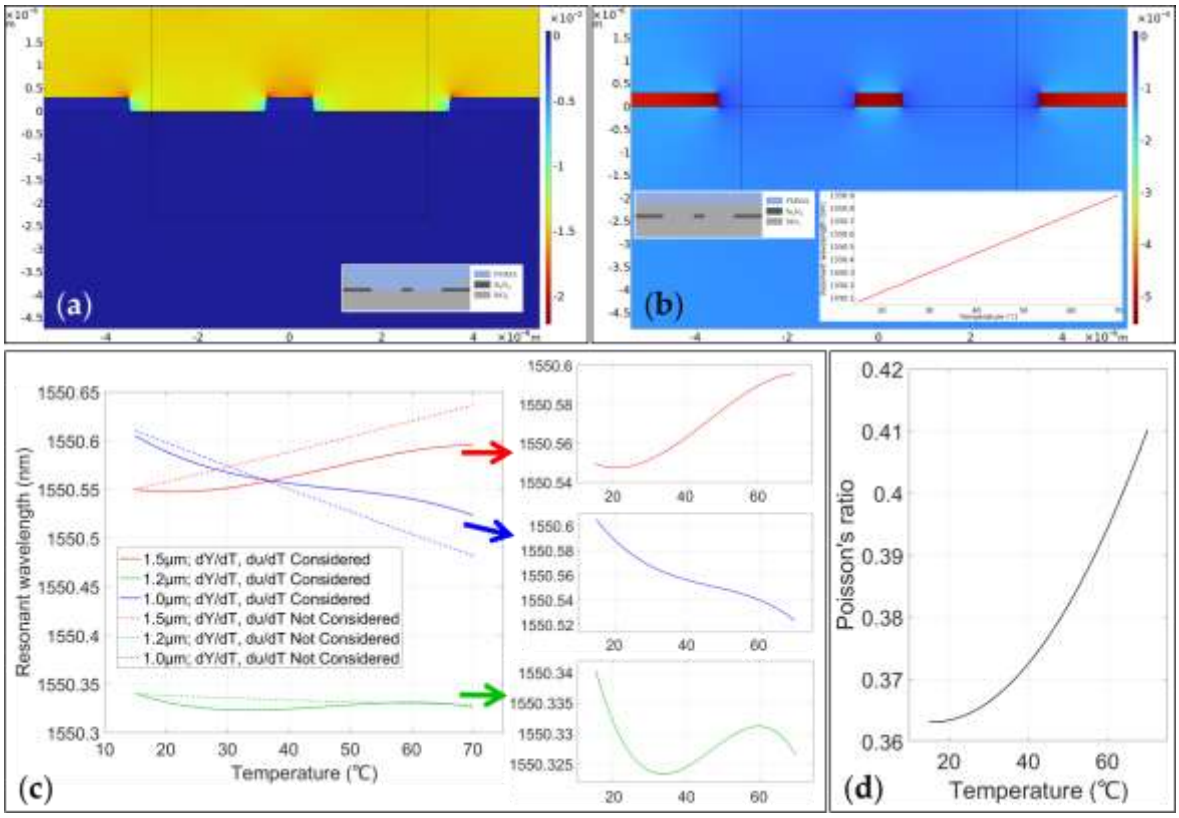


**Figure 4.** Mechanical and electromagnetic field coupled simulation results: (a) Shows the volumetric strain distribution of a silicon nitride waveguide with 1 μm width and PMMA cladding, obtained at 15°C; (b) Presents the volumetric strain distribution of a conventional 1 μm-wide silicon nitride waveguide at 15°C, along with the thermal drift characteristic of microring resonator composed of it; (c) Illustrates the simulated temperature dependence of resonant wavelength for PMMA-cladding waveguide microrings under various conditions, the right side contains magnified views of the nonlinear curves; (d) Displays the temperature dependence of Poisson's ratio for PMMA.

As shown in Figure 4(a), significant thermal strain exists within the PMMA material, and its strain distribution is notably altered by substantial thermal stress caused by severe thermal mismatch. Figure 4(c) presents the simulated temperature characteristics of the resonant wavelength for PMMA-cladding microrings. The simulation results demonstrate that when neglecting the temperature dependence of Young's modulus and Poisson's ratio, the resonant wavelength exhibits nearly linear temperature dependence. In contrast, when incorporating the thermal drift of these material properties, the nonlinear thermal drift behavior observed experimentally is successfully reproduced. Under identical material parameters, the simulation results for different waveguide widths consistently match the experimental trends, demonstrating that the temperature-dependent Young's modulus and Poisson's ratio of PMMA play a crucial role in the observed nonlinear thermal drift phenomenon.

As shown in Figure 4(b), conventional microrings exhibit maximum thermal strain approximately two orders of magnitude smaller than PMMA-cladding microrings. Furthermore, silicon dioxide and silicon nitride possess lower strain-optic coefficients as well as less temperature dependence in Young's modulus and Poisson's ratio. Consequently, their nonlinear thermal drift are negligible, which confirmed in both simulation and experimental results. In summary, when designing athermal microring resonators, the temperature dependence of materials' Young's modulus and Poisson's ratio must be considered.

The nonlinear thermal drift characteristics observed in this study present potential application scenarios. Since one primary function of athermal devices is to address the challenge where thermal control delays fail to meet operational requirements, these devices exhibit rapid temperature

 doi:10.20944/preprints202603.0422.v1



fluctuations within a limited range. This phenomenon enables microring resonators or other optical components to operate within low-drift temperature intervals when minimal thermal drift is required, and within high-drift temperature intervals when thermal tuning is necessary. Such an approach effectively resolves the inherent contradiction between temperature insensitivity and thermal tunability at designated wavelength.

## 5. Conclusions

This study designed and fabricated the temperature-insensitive microring resonators with PMMA claddings. Experimental measurements showed that the temperature-insensitive microring with a waveguide width of 1.5 μm exhibited a maximum absolute thermal drift of only ~2.0 pm/K within the temperature range of 15°C to 70°C. For the nonlinear thermal drift characteristics observed in experiments, simulation analysis revealed that this behavior was primarily attributed to the temperature-dependent Young's modulus and Poisson's ratio of PMMA. Therefore, to suppress the nonlinear thermal drift characteristics of microrings compensated by materials with negative thermo-optic coefficients, one can employ materials exhibiting minimal temperature dependence in both Young's modulus and Poisson's ratio, or alternatively optimize the design to reduce the resultant thermal strain. Additionally, the nonlinear temperature drift phenomenon can also be utilized to achieve switching between an athermal device and a thermal modulator.

**Author Contributions:** Conceptualization, T.Z. and X.W.; methodology, T.Z. and X.W.; software, T.Z.; validation, T.Z., X.W. and M.L.; formal analysis, T.Z., X.W., J.X. and S.L.; investigation, T.Z., R.Y. and X.W.; resources, M.L., X.W. and T.Z.; data curation, T.Z.; writing—original draft preparation, T.Z. and R.Y.; writing—review and editing, T.Z., X.W., J.X. and S.L.; visualization, T.Z.; supervision, M.L. and X.W.; project administration, X.W. and M.L.; funding acquisition, J.X. and S.L. All authors have read and agreed to the published version of the manuscript.".

**Funding:** This work was supported by Ningbo Natural Science Foundation Youth Doctoral Innovation Research Project (2023J397).

**Institutional Review Board Statement:** Not applicable.

**Informed Consent Statement:** Not applicable.

**Data Availability Statement:** Not applicable.

**Conflicts of Interest:** The authors declare no conflict of interest.

## References

1. Zhu, X.; Padmaraju, K.; Luo, L.-W.; Yang, S.; Glick, M.; Dutt, R.; Lipson, M.; Bergman, K. Fast Wavelength Locking of a Microring Resonator. IEEE PHOTONICS TECHNOLOGY LETTERS 2014, 26, 2365–2368.
2. Djordjevic, S.S.; Shang, K.; Guan, B.; Cheung, S.T.S.; Liao, L.; Basak, J.; Liu, H.-F.; Yoo, S.J.B. CMOS-Compatible, Athermal Silicon Ring Modulators Clad with Titanium Dioxide. Opt. EXPRESS 2013, 21, 13958–13968.
3. Guha, B.; Kyotoku, B.B.C.; Lipson, M. CMOS-Compatible Athermal Silicon Microring Resonators. Opt. Express 2010, 18, 3487, doi:10.1364/OE.18.003487.
4. Dell'Olio, F.; Conteduca, D.; Brunetti, G.; Armenise, M.N.; Ciminelli, C. Novel CMOS-Compatible Athermal and Polarization-Insensitive Ring Resonator as Photonic Notch Filter. IEEE Photonics J. 2018, 10, 1–11, doi:10.1109/JPHOT.2018.2877081.
5. Jean, P.; Douaud, A.; Thibault, T.; LaRochelle, S.; Messaddeq, Y.; Shi, W. Sulfur-Rich Chalcogenide Claddings for Athermal and High-Q Silicon Microring Resonators. OPTICAL MATERIALS EXPRESS 2021, 11, 913–925.

 doi:10.20944/preprints202603.0422.v1




6. Lopez-Rodriguez, B.; Sharma, N.; Li, Z.; van der Kolk, R.; van der Boom, J.; Scholte, T.; Chang, J.; Groblacher, S.; Esmaeil Zadeh, I. Magic Silicon Dioxide for Widely Tunable Photonic Integrated Circuits. ACS PHOTONICS 2025, 12, 1321–1328.
7. Sinclair, M.; Gallacher, K.; Sorel, M.; Bayley, J.C.; McBrearty, E.; Millar, R.W.; Hild, S.; Paul, D.J. 1.4 Million Q Factor Si3 N4 Micro-Ring Resonator at 780 Nm Wavelength for Chip-Scale Atomic Systems. Opt. Express 2020, 28, 4010, doi:10.1364/OE.381224.
8. Zhou, L.; Okamoto, K.; Yoo, S.J.B. Towards Athermal Slotted Silicon Microring Resonators with UV-Trimmable PMMA Upper-Cladding. In Proceedings of the Conference on Lasers and Electro-Optics/International Quantum Electronics Conference; OSA: Baltimore, Maryland, 2009; p. CTuBB3.
9. Zhou, L.; Kashiwagi, K.; Okamoto, K.; Scott, R.P.; Fontaine, N.K.; Ding, D.; Akella, V.; Yoo, S.J.B. Towards Athermal Optically-Interconnected Computing System Using Slotted Silicon Microring Resonators and RF-Photonic Comb Generation. Appl. Phys. A 2009, 95, 1101–1109, doi:10.1007/s00339-009-5120-7.
10. Wang, F.; Xu, X.; Sun, C.; Du, L.; Zhao, J. Temperature-Insensitive Second-Order Microring Resonator for Dense Wavelength Division Multiplexing (DWDM). IEEE Photonics J. 2025, 17, 1–7, doi:10.1109/JPHOT.2025.3552080.
11. Chu, S.T.; Wugan Pan; Suzuki, S.; Little, B.E.; Sato, S.; Kokubun, Y. Temperature Insensitive Vertically Coupled Microring Resonator Add/Drop Filters by Means of a Polymer Overlay. IEEE Photon. Technol. Lett. 1999, 11, 1138–1140, doi:10.1109/68.784226.
12. Rakib-Uddin, M.; Won, Y.H. Rib Waveguide-Based Athermal Micro-Ring Resonator. OPTICAL AND QUANTUM ELECTRONICS 2015, 47, 2667–2673.
13. Qiu, F.; Han, Y. Electro-Optic Polymer Ring Resonator Modulators [Invited]. Chin. Opt. Lett. 2021, 19, 041301, doi:10.3788/COL202119.041301.
14. Bian, D.; Chen, S.; Lei, X.; Qin, G.; Chen, Z. Design of a Polymer-Filled Silicon Nitride Strip/Slot Asymmetric Hybrid Waveguide for Realizing Both Flat Dispersion and Athermal Operation. Appl. Opt. 2016, 55, 4827, doi:10.1364/AO.55.004827.
15. Han, P.; He, L.; Xu, L.; Zhang, L. Athermal Waveguides and Resonators with Three Zero-Thermal-Drift Wavelengths. J. Nanophoton. 2023, 17, doi:10.1117/1.JNP.17.046005.
16. Takai, Y.; Tsuda, H. Athermal Silicon Optical Circuit Using Half-Etched Core and Silicone. In Proceedings of the Silicon Photonics XIX; Reed, G.T., Knights, A.P., Eds.; SPIE: San Francisco, United States, March 12 2024; p. 19.
17. Lei, X.; Bian, D.; Chen, S. A Proposal for the Generation of Optical Frequency Comb in Temperature Insensitive Microcavity. Chinese Phys. B 2016, 25, 114214, doi:10.1088/1674-1056/25/11/114214.
18. Fauser D.; Rodríguez Agudo J.A.; Steeb H. Direct and Indirect Measurement of Complex Poisson's Ratio—Indirect Measurement in Torsion and Tension 2024.
19. Roselló-Mechó, X.; Delgado-Pinar, M.; Díez, A.; Andrés, M.V. Measurement of the Strain-Optic Coefficients of PMMA from 800 to 2000 Nm. OSA Continuum 2020, 3, 441, doi:10.1364/OSAC.384509.